



## Large current density for oxygen evolution from pyramidal-coordinated Co oxide

Yitian Hu<sup>a,b,1</sup>, Lili Li<sup>c,1</sup>, Jianfa Zhao<sup>d</sup>, Yu-Cheng Huang<sup>e</sup>, Chang-yang Kuo<sup>f</sup>, Jing Zhou<sup>a</sup>, Yalei Fan<sup>a</sup>, Hong-Ji Lin<sup>f</sup>, Chung-Li Dong<sup>e</sup>, Chih-Wen Pao<sup>f</sup>, Jyh-Fu Lee<sup>f</sup>, Chien-Te Chen<sup>f</sup>, Changqing Jin<sup>d</sup>, Zhiwei Hu<sup>g,\*</sup>, Jian-Qiang Wang<sup>a,b,h,\*\*</sup>, Linjuan Zhang<sup>a,b,h,\*\*</sup>

<sup>a</sup> Key Laboratory of Interfacial Physics and Technology, Shanghai Institute of Applied Physics, Chinese Academy of Sciences, Shanghai 201800, China

<sup>b</sup> University of Chinese Academy of Sciences, Beijing 100049, China

<sup>c</sup> State Key Lab of Crystal Materials and Institute of Crystal Materials, Shandong University, Jinan 250100, China

<sup>d</sup> Beijing National Laboratory for Condensed Matter Physics Institute of Physics Chinese Academy of Sciences, Beijing 100190, China

<sup>e</sup> Department of Physics, Tamkang University, 151 Yingzhan Rd., New Taipei City 25137, Taiwan, R.O.C

<sup>f</sup> National Synchrotron Radiation Research Center, Hsinchu 30076, Taiwan, R.O.C

<sup>g</sup> Max Planck Institute for Chemical Physics of Solids, Nöthnitzer Strasse 40, Dresden 01187, Germany

<sup>h</sup> Dalian National Laboratory for Clean Energy, Dalian 116023, China

### ARTICLE INFO

#### Keywords:

BiCoO<sub>3</sub>  
Oxygen evolution reaction  
Large current density  
Oxygen vacancies

### ABSTRACT

Developing efficient electrocatalyst at large current densities to meet the requirement of industrial water splitting is a big challenge today. Herein, we report a class of catalyst, BiCoO<sub>3</sub> with pyramidal-coordinated Co<sup>3+</sup>. BiCoO<sub>3</sub> exhibits a large current density of 1000 mA cm<sup>-2</sup> at a low overpotential of 402 mV and the overpotential even reduces to only 303 mV to achieve 1000 mA cm<sup>-2</sup> by replacing Co with Fe, which belongs to the first-class level among large-current-densities electrocatalysts reported so far. Different from artificially created oxygen vacancies to optimize the bonding strength of the intermediate for enhancement of OER activity, BiCoO<sub>3</sub> has the rich active sites and the shortest reaction pathway leading to a large current density, as structurally every Co-O cluster has one oxygen vacancy. This work opens a new avenue for enhanced OER activity at high current densities via optimizing the arrangement of ligand vacancies.

### 1. Introduction

The development of renewable green energy sources is rapidly becoming a key instrument in addressing various energy and environmental problems [1]. In this context, the oxygen evolution reaction (OER) has emerged as a critical reaction in electrochemical energy storage and conversion processes, including fuel cells, metal-air batteries and water splitting [2]. However, the multistep proton-coupled electron transfer processes constituting the OER have hindered improvements in the efficiency of this electrochemical system [3]. A large number of electrocatalysts have been studied for OER reactions, but most of them show good performance only at relatively low current densities (< 20 mA cm<sup>-2</sup>), which cannot meet the high current densities

(> 500 mA cm<sup>-2</sup>) requirements for industrial electrochemical applications [4]. Under high current densities, the massive accumulation of gas bubbles can drastically slow the charge and mass transfers of electrode and decrease the exposure of active sites, resulting in the exorbitant overpotentials, and thus higher requirements were put forward for high-current-density OER catalysts [5]. At present, noble metal including Ir-based and Ru-based catalyst belong to the level of state-of-the-art OER electrocatalysts for their high intrinsic activity and low activation energy barrier [6], but their scarcity and high cost hinder their large-scale application. In order to address such issues, highly efficient and earth-abundant catalysts are urgently required to realize the operation under large current densities.

Thus, tremendous efforts have been spent on developing transition

\* Corresponding author.

\*\* Corresponding author at: Key Laboratory of Interfacial Physics and Technology, Shanghai Institute of Applied Physics, Chinese Academy of Sciences, Shanghai 201800, China.

E-mail addresses: [Zhiwei.Hu@cpfs.mpg.de](mailto:Zhiwei.Hu@cpfs.mpg.de) (Z. Hu), [wangjianqiang@sinap.ac.cn](mailto:wangjianqiang@sinap.ac.cn) (J.-Q. Wang), [zhanglinjuan@sinap.ac.cn](mailto:zhanglinjuan@sinap.ac.cn) (L. Zhang).

<sup>1</sup> Y.H. and L.L. contributed equally to this work.

metal-based compounds which are appealing and promising electrocatalysts for the OER at high current densities. Recently, diverse strategies have been explored to enhance the large-current-density OER activity. For example, the high-curvature tips on  $\text{Ni}_x\text{Fe}_{1-x}$  alloy nancones arrays were adopted to enhance the local electric field and thus accelerate the mass transfer of reactants, resulting in enhanced OER performance at large current [7]. A Schottky heterojunction, which consisted of NiFe hydroxide nanoparticles and ultrathin NiS nanosheets ( $\text{NiFe LDH}/\text{NiS}$ ), performed well at the high current densities due to the rich porosity of NiS nanosheets and interfacial effect of Schottky heterojunction [8]. A hierarchical Ni–Fe oxyhydroxide@NiFe alloy nanowire array was reported with exceptional performance at high current densities due to the improved charge and mass transfer [9]. The dual-phase  $\text{Co}_2\text{P}-\text{Co}_3\text{O}_4$  catalyst was served as a good OER electrocatalyst at industrial current densities via synergizing the advantages of two phase components and improving conductivity of  $\text{Co}_3\text{O}_4$  by  $\text{Co}_2\text{P}$  [10]. Beyond those, surface engineering [11] such as vacancy engineering is also a vital strategy to promote the OER activity [12,13]. The hierarchical  $\text{Co}_3\text{O}_4/\text{CoO}$  nanowires@Cu micro-pillars were designed with abundant oxygen vacancies to achieve the industrially required large current and were revealed that the oxygen vacancies can promote the adsorption of intermediate [14]. Nevertheless, there are still some fatal deficiencies when applied to industrial water splitting. Taken the multiphase electrocatalysts for example, the fabrication of such composites involves complicated engineering [15], and the synthesis conditions of the hybrid are prohibitively difficult to manipulate and thus result in excess cost. As for the vacancy engineering, it is known that the artificial creation of oxygen vacancies is often uncontrollable, and the introduction of large numbers of oxygen vacancies can result in amorphous crystal structures, and even transformation into other species under the OER conditions. Therefore, the development of a catalyst

which is simultaneously equipped with an inherently lower site symmetry with a stable crystal structure under high current conditions and simple composition is crucial to speed up the application of industrial water splitting. However, these materials have received little attention to date.

Herein, we report a simple single-phase  $\text{BiCoO}_3$  perovskite with good activity at industrial large current densities, in which the Co ions intrinsically possess lower site symmetry and pyramidally coordinated to five oxygen ions. Simultaneously, this system can be a suitable structural model with ordered arrangement of oxygen vacancies (namely from  $\text{CoO}_6$  to  $\text{CoO}_5$ ) for assessing the OER mechanism. In addition, this is the first report of the in-depth study of  $\text{BiCoO}_3$  perovskite in the water oxidation reaction. In this study, Our  $\text{BiCoO}_3$  catalyst exhibited a 20-fold improvement in mass activity when compared to  $\text{LaCoO}_3$  with  $\text{CoO}_6$  octahedra which exists at the top level of the OER volcano plot [16,17]. Furthermore,  $\text{BiCoO}_3$  can yield high current densities at low overpotentials ( $\eta_{500}=391 \text{ mV}$ ,  $\eta_{1000}=402 \text{ mV}$ ). The catalyst even drives the current density of  $1000 \text{ mA cm}^{-2}$  at a relatively low overpotential of  $303 \text{ mV}$  by replacing Co with Fe. It was found that the 100% content of ordered oxygen vacancies of  $\text{CoO}_5$  in  $\text{BiCoO}_3$  can provide adequate active sites and the shortest reaction pathway, leading to excellent large current densities. Our first principle theory indicates that  $\text{Co}^{3+}\text{O}_5$  coordination has lower overpotential than  $\text{Co}^{3+}\text{O}_6$  coordination. Moreover, configuration-interaction cluster calculations reveal that high-spin  $\text{Co}^{3+}$  ion in  $\text{BiCoO}_3$  is quite stable.

## 2. Results and discussion

### 2.1. Structural characterization of pristine $\text{BiCoO}_3$

Ideal perovskite  $\text{BiCoO}_3$  consists of an ordered arrangement of

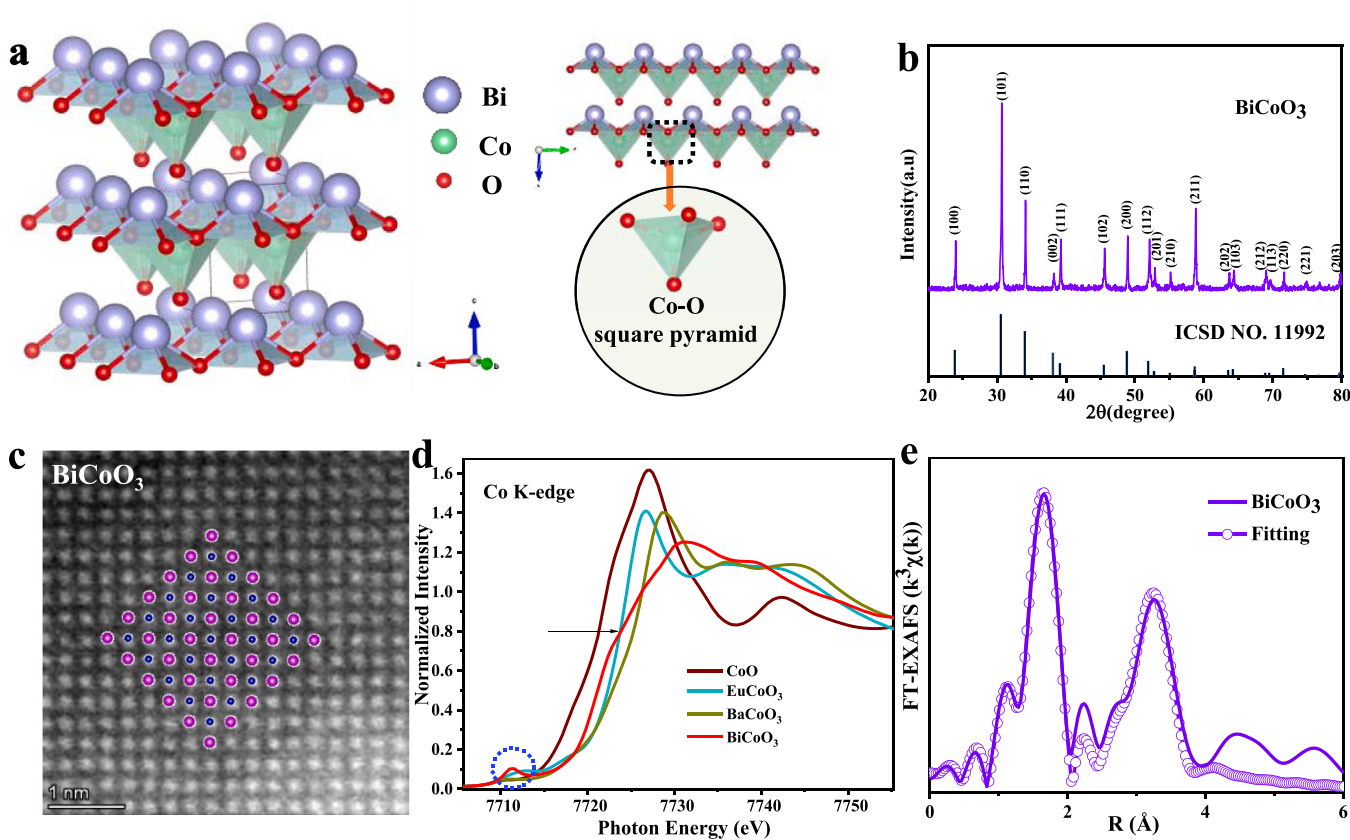


**Fig. 1.** a) Crystal structure of  $\text{BiCoO}_3$ . b) XRD pattern of  $\text{BiCoO}_3$ . c) Atomic-resolution HAADF-STEM image of  $\text{BiCoO}_3$ . The blue and carmine dots represent the Co and Bi atoms, respectively. d) Co K-edge XANES spectra for  $\text{BiCoO}_3$ ,  $\text{CoO}$ ,  $\text{EuCoO}_3$ , and  $\text{BaCoO}_3$ . e) The EXAFS fitting curves for  $\text{BiCoO}_3$ .

corner-shared  $\text{CoO}_5$  square pyramids and  $\text{BiO}_4$  chains (Fig. 1a). The  $\text{BiCoO}_3$  sample was successfully prepared using a solid-state reaction method [18], and its structure and morphology were characterized by X-ray diffraction (XRD) and transmission electron microscopy (TEM). As shown in Fig. 1b, the XRD pattern of  $\text{BiCoO}_3$  corresponded well with the standard pattern of the  $P4mm$  space group, wherein no observable impurity phases were present, and Rietveld refinement analysis also performed in Fig. S1 and Table S1. The well-defined structure of  $\text{BiCoO}_3$  was also demonstrated by high-angle annular dark-field scanning transmission electron microscopy (HAADF-STEM) imaging (Fig. 1c). The selected-area electron diffraction (SAED) pattern of  $\text{BiCoO}_3$  recorded along with [001] zone axis was shown in Fig. S2, indicating the good crystallinity of this catalyst. The particle size of  $\text{BiCoO}_3$  (Fig. S3a) and atomic arrangement of the catalyst were investigated using TEM and high-resolution TEM (HRTEM), respectively. More specifically, clear lattice fringes (distance = 0.28 nm) belonging to the (101) crystal planes were observed in the prepared  $\text{BiCoO}_3$  specimen (Fig. S3b). In addition, as shown in Fig. S4, Bi, Co, and O were distributed homogeneously throughout the sample. The morphology and element content of sample  $\text{BiCoO}_3$  were characterized by scanning electron microscope (SEM) (Fig. S5) and energy-dispersive X-ray (EDX) (Fig. S6) spectroscopy, respectively. It is shown that  $\text{BiCoO}_3$  presents a scattered structure and the atomic ratio of Bi/Co/O is in agreement with the expected stoichiometry. Furthermore, the electronic and local structures of  $\text{BiCoO}_3$  were studied using Co K-edge X-ray absorption spectroscopy (XAS). It is well known that the K-edge X-ray absorption near-edge structures (XANES) of 3d transition metals are particularly sensitive to their valence states [11,19,20]. Fig. 1d shows the Co-K XANES spectra of  $\text{BiCoO}_3$ , along with those of  $\text{CoO}$ ,  $\text{EuCoO}_3$ , and  $\text{BaCoO}_3$  for comparison. It can be seen from the spectra that the energy position of the Co-K absorption edge (at a normalized intensity of 0.8) for  $\text{BiCoO}_3$  was similar to that of  $\text{EuCoO}_3$ , suggesting a valence state of approximately +3. It should be noted that the XANES profile of  $\text{BiCoO}_3$  deviates from that of  $\text{EuCoO}_3$  owing to their

different coordinate environments, i.e., a  $\text{CoO}_5$  coordination structure in  $\text{BiCoO}_3$  and a  $\text{CoO}_6$  coordination structure in  $\text{EuCoO}_3$ . In addition, the intensity of the pre-edge peak depends on the structural symmetry of the molecule and increases as the molecule deviates from centrosymmetry [21], so the larger pre-peak intensity of Co-K XANES in  $\text{BiCoO}_3$  compared to that in  $\text{EuCoO}_3$  confirms the decreasing structural symmetry upon from the  $\text{CoO}_6$  to the  $\text{CoO}_5$  coordination structure. Extended X-ray absorption fine structure (EXAFS) [22,23] and wavelet transform (WT) contour analyses were further adopted to investigate the coordination environment of the prepared specimen (Fig. 1e and S7). Based on the quantitative details obtained by EXAFS fitting (Table S2), it is clear that Co adopts a  $\text{CoO}_5$  coordination structure in the  $\text{BiCoO}_3$  sample with average Co–O bond length of ~2.00 Å.

## 2.2. Evaluation of the electrochemical performance

To assess the electrocatalytic OER activity of the  $\text{BiCoO}_3$  sample containing a unique  $\text{CoO}_5$  pyramid-type structure, linear sweep voltammetry (LSV) was carried out in an  $\text{O}_2$ -saturated 1.0 M KOH solution at a rotation speed of 1600 rpm and a scan rate of 5 mV s<sup>-1</sup>. The potential was controlled using a standard three-electrode system and was referenced to the reversible hydrogen electrode (RHE). Here,  $\text{LaCoO}_3$  and  $\text{EuCoO}_3$  are chosen as the reference, because that both of them have  $\text{CoO}_6$  cluster while it is different from the HS state in  $\text{BiCoO}_3$  [18] that HS/LS state mixture exist in  $\text{LaCoO}_3$  [24–28] and LS state exist in  $\text{EuCoO}_3$  [24,29,30]. Upon examination of the LSV curves in Fig. 2a, it became clear that  $\text{BiCoO}_3$  exhibited significantly enhanced OER activity compared with  $\text{EuCoO}_3$  and  $\text{LaCoO}_3$  requiring only a low overpotential of 302 mV to afford a current density of 10 mA cm<sup>-2</sup>, which is much superior to those of  $\text{EuCoO}_3$  (407 mV),  $\text{LaCoO}_3$  (430 mV), or benchmark  $\text{IrO}_2$  (313 mV). Subsequently, the mass activities (MA) of the  $\text{BiCoO}_3$ ,  $\text{EuCoO}_3$ ,  $\text{LaCoO}_3$ , and  $\text{IrO}_2$  catalysts were compared at an overpotential of 300 mV in Fig. 2b.  $\text{BiCoO}_3$  exhibited the highest MA of 44.69 A g<sup>-1</sup>,

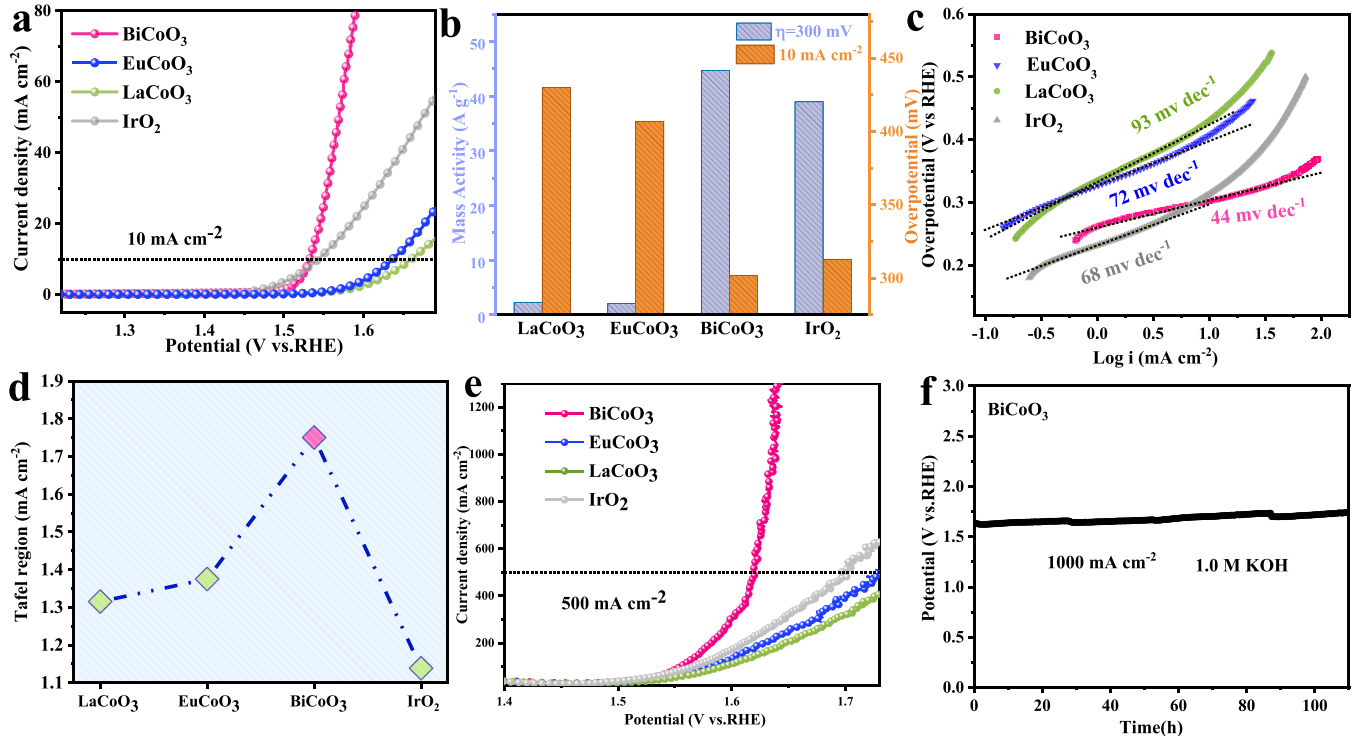


**Fig. 2.** a) LSV curves of  $\text{BiCoO}_3$ ,  $\text{EuCoO}_3$ ,  $\text{LaCoO}_3$ , and  $\text{IrO}_2$ . b) Comparison between the overpotentials ( $10 \text{ mA cm}^{-2}$  current density) and mass activities (300 mV overpotential) of the  $\text{BiCoO}_3$ ,  $\text{EuCoO}_3$ ,  $\text{LaCoO}_3$ , and  $\text{IrO}_2$  specimens. c) Tafel slope plots of  $\text{BiCoO}_3$ ,  $\text{EuCoO}_3$ ,  $\text{LaCoO}_3$ , and  $\text{IrO}_2$ . d) Comparison of the length of Tafel linear region for  $\text{BiCoO}_3$ ,  $\text{EuCoO}_3$ ,  $\text{LaCoO}_3$ , and  $\text{IrO}_2$ . e) OER LSV curves for  $\text{BiCoO}_3$ ,  $\text{EuCoO}_3$ ,  $\text{LaCoO}_3$ , and  $\text{IrO}_2$  under the high current densities after coating on nickel foam. f) Measurement of the long-term electrochemical stability of  $\text{BiCoO}_3$  at a current density of  $1000 \text{ mA cm}^{-2}$ .

which is ~21 times higher than that of EuCoO<sub>3</sub> and ~20 times higher than that of LaCoO<sub>3</sub>. Furthermore, Tafel analysis was performed to gain insight into the kinetics of the OER (Fig. 2c), and it was found that BiCoO<sub>3</sub> displays the smallest Tafel slope of 44 mV dec<sup>-1</sup> compared to the corresponding values of 68, 72, and 93 mV dec<sup>-1</sup> obtained for IrO<sub>2</sub>,

EuCoO<sub>3</sub>, and LaCoO<sub>3</sub>, respectively. Electrochemical impedance spectroscopy (EIS) was also performed to evaluate the charge-transfer resistances of the samples (Fig. S8) to confirm the faster degree of charge transfer in BiCoO<sub>3</sub>. Meanwhile, the electrochemical active surface area (ECSA) was determined by collecting cyclic voltammetry (CV) data in

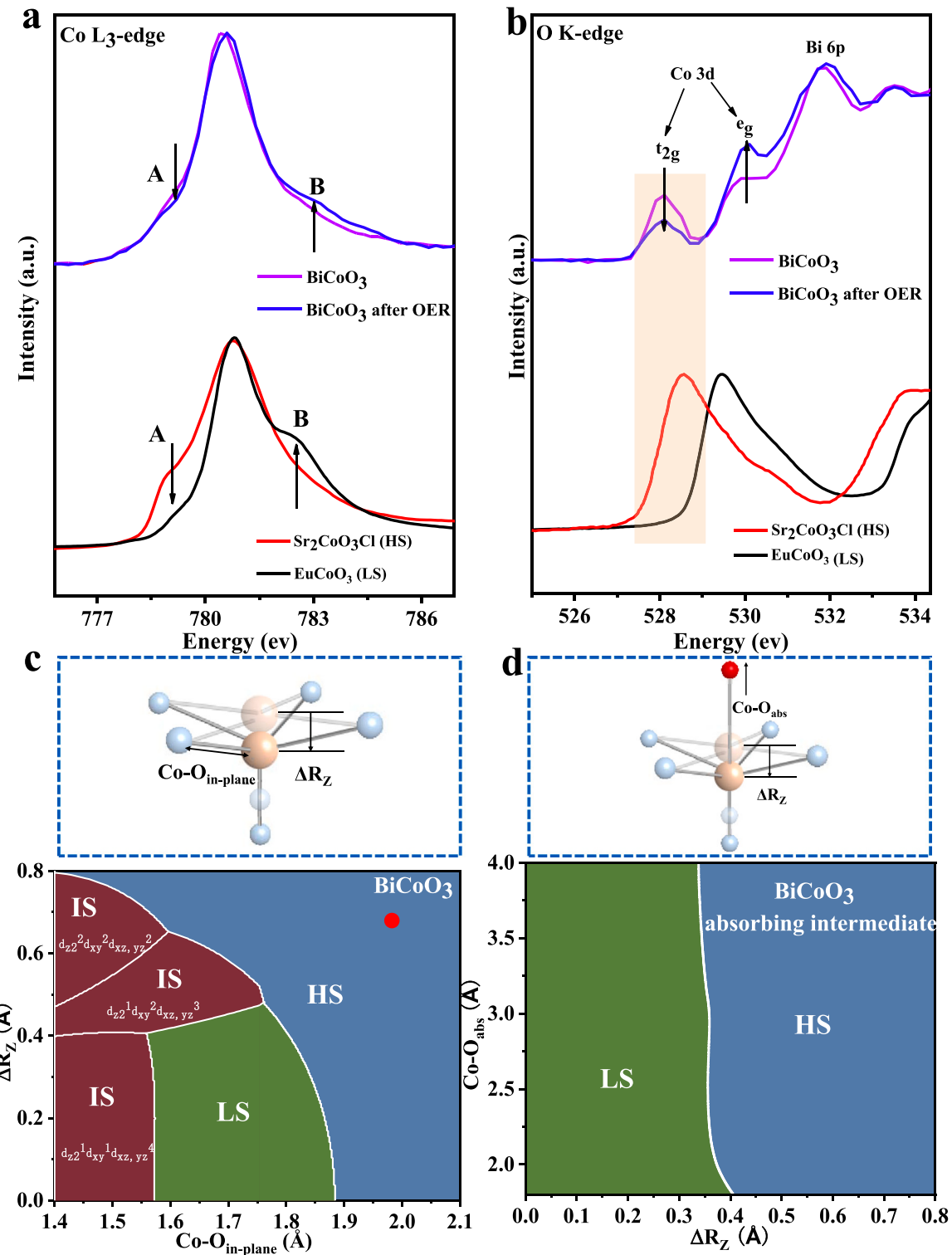


**Fig. 3.** Comparison of a) the Co L<sub>3</sub>-edge and b) the O K-edge sXAS spectra of BiCoO<sub>3</sub> before and after the OER. The spectra of Sr<sub>2</sub>CoO<sub>3</sub>Cl and EuCoO<sub>3</sub> are also shown as reference HS-Co<sup>3+</sup> and LS-Co<sup>3+</sup>, respectively. c) The phase diagram of the spin state of Co<sup>3+</sup> as a function of in-plane Co-O bond length and out-of-plane Co displacement ( $\Delta R_Z$ ) for BiCoO<sub>3</sub>. d) The phase diagram of the spin state of Co<sup>3+</sup> as a function of  $\Delta R_Z$  and the bond length between Co and intermediate species (Co-O<sub>abs</sub>) in BiCoO<sub>3</sub>. The corresponding two schematics of the cluster-structure changes are shown on top, respectively. (Orange spheres, cobalt; blue, oxygen; red, intermediate species.).

the non-Faraday region (Fig. S9), wherein the ECSA was positively correlated with the electrochemical double-layer capacitance ( $C_{dl}$ ). As shown in Fig. S10a, the  $C_{dl}$  of BiCoO<sub>3</sub> was determined to be ~15 and ~12 times larger than those of EuCoO<sub>3</sub> and LaCoO<sub>3</sub>, respectively, revealing the largest ECSA and a greater number of electrochemically active sites for BiCoO<sub>3</sub>, which are beneficial for catalyzing OER process. LSVs curves were further normalized by ECSA to investigate the intrinsic factor for water oxidation (Fig. S10b), and BiCoO<sub>3</sub> exhibited the highest intrinsic activity. When compared to other reported Co-based oxide electrocatalysts, such as oxyhydroxides, perovskite, metallic oxides, and spinel species, the activity of BiCoO<sub>3</sub> was found to be superior as shown in Table S3.

For industrial applications, water electrolysis needs to meet the strict criteria of achieving extremely large current densities ( $>500 \text{ mA cm}^{-2}$ ) at low overpotentials [31], thus the possibility of industrial-scale application for our catalyst BiCoO<sub>3</sub> was further evaluated. It is known that when the current density is high, the fast formation of bubbles would block the diffusion of electrolyte and the concentration polarization dominates the electrochemical process accompanied by excess overpotential and increased slop in the Tafel plots [32]. Thus, the length of Tafel linear region as a parameter was introduced to evaluate the OER process of different catalysts (Fig. 2d). Compared to IrO<sub>2</sub>, EuCoO<sub>3</sub>, and LaCoO<sub>3</sub>, BiCoO<sub>3</sub> peaks in the chart and maintains a constant slope until the higher current density, revealing the diminished concentration polarization for BiCoO<sub>3</sub> and thus leading to much less overpotentials needed to achieve large current densities. In order to directly verify that, the large-current-density OER performance of BiCoO<sub>3</sub> were evaluated and compared with that of EuCoO<sub>3</sub>, LaCoO<sub>3</sub>, and IrO<sub>2</sub> by coating the catalysts on the nickel foam supporting electrode (Fig. 2e). Very impressively, the activity of BiCoO<sub>3</sub> becomes superior under high current densities and can drive the industry-level large current of 500 and 1000 mA cm<sup>-2</sup> at overpotentials of only 391 mV and 402 mV respectively, and far outperforms the reference samples. Moreover, due to the importance of a long-term catalytic stability in the OER, stability tests were performed for BiCoO<sub>3</sub> at an extremely large current density of 1000 mA cm<sup>-2</sup>. As shown in Fig. 2f, the relatively constant activity of catalyst indicates that this catalyst exhibits a good stability. The above results demonstrate that we have found a wonderful material of BiCoO<sub>3</sub> suitable for OER at high current densities and further get the exceptional activity by optimization in a later section.

### 2.3. Evolution of electronic structure

It is known that electrochemical reactions typically occur within ~5 nm of the catalyst surface region [33,34]. Thus, to understand the structural origin of OER activity for BiCoO<sub>3</sub>, the catalyst before and after OER was studied using surface-sensitive soft XAS (sxAS) at the Co-L<sub>3</sub> and O-K edges, which are highly sensitive to the valence states [27,35], spin states [36], and local environments [37,38] of the Co ions and unoccupied O-2p states [39]. The Co L<sub>3</sub>-edge sxAS spectra of BiCoO<sub>3</sub> before and after the OER are shown in Fig. 3a. For comparison, Sr<sub>2</sub>CoO<sub>3</sub>Cl and EuCoO<sub>3</sub> were selected as reference specimens for HS-Co<sup>3+</sup> and LS-Co<sup>3+</sup>, respectively [24]. One can see that the energy position and spectral shape of BiCoO<sub>3</sub> are comparable to those of the HS-Co<sup>3+</sup> reference, revealing a valence state of + 3 and a pure HS state for the Co ions in BiCoO<sub>3</sub>, which is fully consistent with previous research [18]. However, after the OER, one can see clear change of multiplet spectral feature: the spectral weight of the lower energy shoulder (denoted A) below the main decreases, while the spectral weight of the higher shoulder (denoted B) above the main increases. The similar trend can be observed in the comparison between Sr<sub>2</sub>CoO<sub>3</sub>Cl (HS-Co<sup>3+</sup>) and EuCoO<sub>3</sub> (LS-Co<sup>3+</sup>) as shown in Fig. 3a, however the spectral change from HS-Co<sup>3+</sup> to LS-Co<sup>3+</sup> is much significant as compared with change observed before and after OER for BiCoO<sub>3</sub>. This small LS-Co<sup>3+</sup> spectral weight in BiCoO<sub>3</sub> has also been observed, but disappeared if the fresh surface was obtained under ultrahigh vacuum condition [40]. Thus, we can conclude that the

top layers become LS-Co<sup>3+</sup> after OER.

Occurrence of LS-Co<sup>3+</sup> at surface after OER is also expected to be observed in the O-K edge. The pre-edge peaks below 531.5 eV as shown in Fig. 3b are assigned to transition from O1s core level to unoccupied O2p state due to the covalent hybridization between the unoccupied O 2p orbitals and the 3d transition metal states [41]. The O-K edge sxAS of the BiCoO<sub>3</sub> before and after the OER, along with those of Sr<sub>2</sub>CoO<sub>3</sub>Cl and EuCoO<sub>3</sub> references are shown in Fig. 3b. The strong peak located at 532 eV is related to Bi-6p states [18]. Here, we concentrate on the pre-edge peak below 531.5 eV. In the spectrum of EuCoO<sub>3</sub>, a single pre-edge peak is present at ~529.4 eV, which was assigned to the transition from the O 1s core level to the e<sub>g</sub> orbitals, since the t<sub>2g</sub> orbitals are fully occupied for LS-Co<sup>3+</sup> for EuCoO<sub>3</sub> [18] and transitions only to the e<sub>g</sub> orbitals are possible. In case of HS-Co<sup>3+</sup>, the transition from the O 1s core level to the t<sub>2g</sub> orbitals become possible giving rise of lower energy pre-edge peak ~528.5 eV in the spectrum of Sr<sub>2</sub>CoO<sub>3</sub>Cl [18]. For the pristine BiCoO<sub>3</sub>, the clear peaks observed at ~528 and ~530 eV at the O-K edge can be indexed to the unoccupied t<sub>2g</sub>- and e<sub>g</sub>-related states of HS-Co<sup>3+</sup>, respectively [40]. However, after the OER, the relative spectral intensity of the peak at ~528 eV decreased. The similar change was also observed and assigned to small content of LS-Co<sup>3+</sup>, further confirming the spin state transformation of the surface Co<sup>3+</sup> ions during the OER. It is noteworthy that the peak at ~528 eV does not disappear even in the surface sensitive TEY mode. This implies that only very thin top layer of Co<sup>3+</sup> ions in the BiCoO<sub>3</sub> becomes LS after the OER.

In order to set forth the origin concerning the spin state evolution, we performed configuration-interaction cluster calculations to study the relationship between the coordination structure and the spin state of Co<sup>3+</sup> ions [29]. Based on the detailed structure of BiCoO<sub>3</sub> [42], the spin state of Co<sup>3+</sup> as a function of in-plane Co-O bond length (Co-O<sub>in-plane</sub>) and out-of-plane Co displacement ( $\Delta R_z$ ) are investigated. As shown in Fig. 3c, BiCoO<sub>3</sub> locates at the region of HS (red dot) and far away from any spin-state transition point, which is consistent with the result of Co L<sub>2,3</sub>-edge XAS for as-prepared BiCoO<sub>3</sub>, and indicate that HS Co<sup>3+</sup> in BiCoO<sub>3</sub> is quite stable and hardly transform to other spin states. Considering that during OER the surface Co will adsorb intermediate species (such as OH\*, O\*, OOH\*, etc) to form CoO<sub>6</sub>, we further consider the case of Co<sup>3+</sup> for CoO<sub>6</sub> coordination structure. Base on the configuration-interaction cluster calculation, the Co<sup>3+</sup> spin state of CoO<sub>6</sub> as a function of  $\Delta R_z$  and the distance between Co and additional adsorbed O ions (Co-O<sub>abs</sub>) are shown in Fig. 3d. Here, we assume that there is no change of the lattice parameters along x and y directions due to the restrictive effect of the bulk. Compared with CoO<sub>5</sub>, the existence of additional O atom in z-axis in CoO<sub>6</sub> will significantly decrease the displacement of Co ions leaving the xy plane (Fig. S11), which will significantly increase the energy splitting between the e<sub>g</sub> and t<sub>2g</sub> shells and decrease the splitting between d<sub>xz</sub><sup>2</sup> and d<sub>yz</sub><sup>2</sup>, thus induce LS states. It is worth noting that the decrease of  $\Delta R_z$  is a more important factor to stabilize LS than the distance of Co-O<sub>abs</sub>, for which when  $\Delta R_z$  is smaller than 0.32 Å, the LS is stable even for R(Co-O<sub>abs</sub>) reached to ~4 Å.

Therefore, based on the above theoretical analysis, we could conclude that the evolution of Co<sup>3+</sup> spin state observed in Fig. 3a/b is mainly from the increased oxygen-coordination around Co<sup>3+</sup>, induced by the intermediate species adsorption process during OER. This results also indicate that there are no further oxygen vacancies appeared during the OER, which imply that the lattice oxygen may not participate in the reaction for BiCoO<sub>3</sub>. Simultaneously, isotope labeling experiments, including in situ Raman spectroscopy and differential electrochemical mass spectrometry (DEMS), can also exclude the absence of lattice oxygen participation in BiCoO<sub>3</sub> during the OER (Fig. S12 and S13).

In addition, the robustness of the crystal structure and the surface atomic arrangement of BiCoO<sub>3</sub> after the OER were also determined using XRD, Raman spectroscopy, and TEM. Fig. S14 displays the XRD pattern of BiCoO<sub>3</sub> after the OER, where no impurity can be observed, revealing that the structure of BiCoO<sub>3</sub> remained unchanged after the OER. Fig. S15

shows the Raman spectra of BiCoO<sub>3</sub> before and after the OER, confirming the negligible structural changes of BiCoO<sub>3</sub> during the OER. Furthermore, HRTEM images (Fig. S16) shows the well-defined lattice fringes in the surface area of BiCoO<sub>3</sub> after the OER, indicating the excellent stability of the ordered BiCoO<sub>3</sub> structure. Considering the above results, it is apparent that the prepared BiCoO<sub>3</sub> exhibits an excellent crystallinity and retains its perfect configuration of CoO<sub>5</sub> even after the OER.

#### 2.4. DFT calculation for exploring the OER mechanism

To understand the OER mechanism, the density functional theory (DFT) approach was employed to calculate the Gibbs free energy differences ( $\Delta G$ ) of the OER reaction steps in BiCoO<sub>3</sub>. For low-valence Co<sup>3+</sup> oxides, the most favorable scenario of the reaction mechanism is the metal site adsorbate evolution (MAE) mechanism, which considers only the metal site as the active center instead of lattice oxygen (Fig. S17). For comparison, EuCoO<sub>3</sub> with the same Co<sup>3+</sup> valence state but Co<sub>6</sub> coordination structure was also considered. The optimized structures of the

OER adsorption intermediate corresponding to the MAE steps for BiCoO<sub>3</sub> and EuCoO<sub>3</sub> were shown in Fig. 4b and Fig. S18, respectively. In the mechanism of MAE, Co ions on the surface of both BiCoO<sub>3</sub> and EuCoO<sub>3</sub> will experience similar local structural transformation, however, Co ions in the subsurface still keep in the HS states in BiCoO<sub>3</sub> and LS states in EuCoO<sub>3</sub>, respectively. As shown in Fig. 4a, the MAE scenario of BiCoO<sub>3</sub> has an overpotential ( $\eta$ ) of 0.59 V, lower than that of EuCoO<sub>3</sub> ( $\eta = 0.82$  V), which is consistent with the results of experimental activities. Notably, the rate-limiting step also change from the deprotonation of OH\* for EuCoO<sub>3</sub> to the adsorption of OH\* for BiCoO<sub>3</sub>. Such obvious differences indicate that the difference in the subsurface layer can intrinsically boost the catalytic activity. To clarify the effect of the subsurface, charge density difference and the corresponding plane-integrated along the vertical direction are calculated for BiCoO<sub>3</sub> and EuCoO<sub>3</sub> (Fig. S19), respectively. The results clearly indicate that compared to EuCoO<sub>3</sub>, there exist obvious charge transfer from the surface layer to subsurface layer in BiCoO<sub>3</sub>, which induced more electron gather on the surface, thus affecting the energy of adsorption and deprotonation process of OH\*.

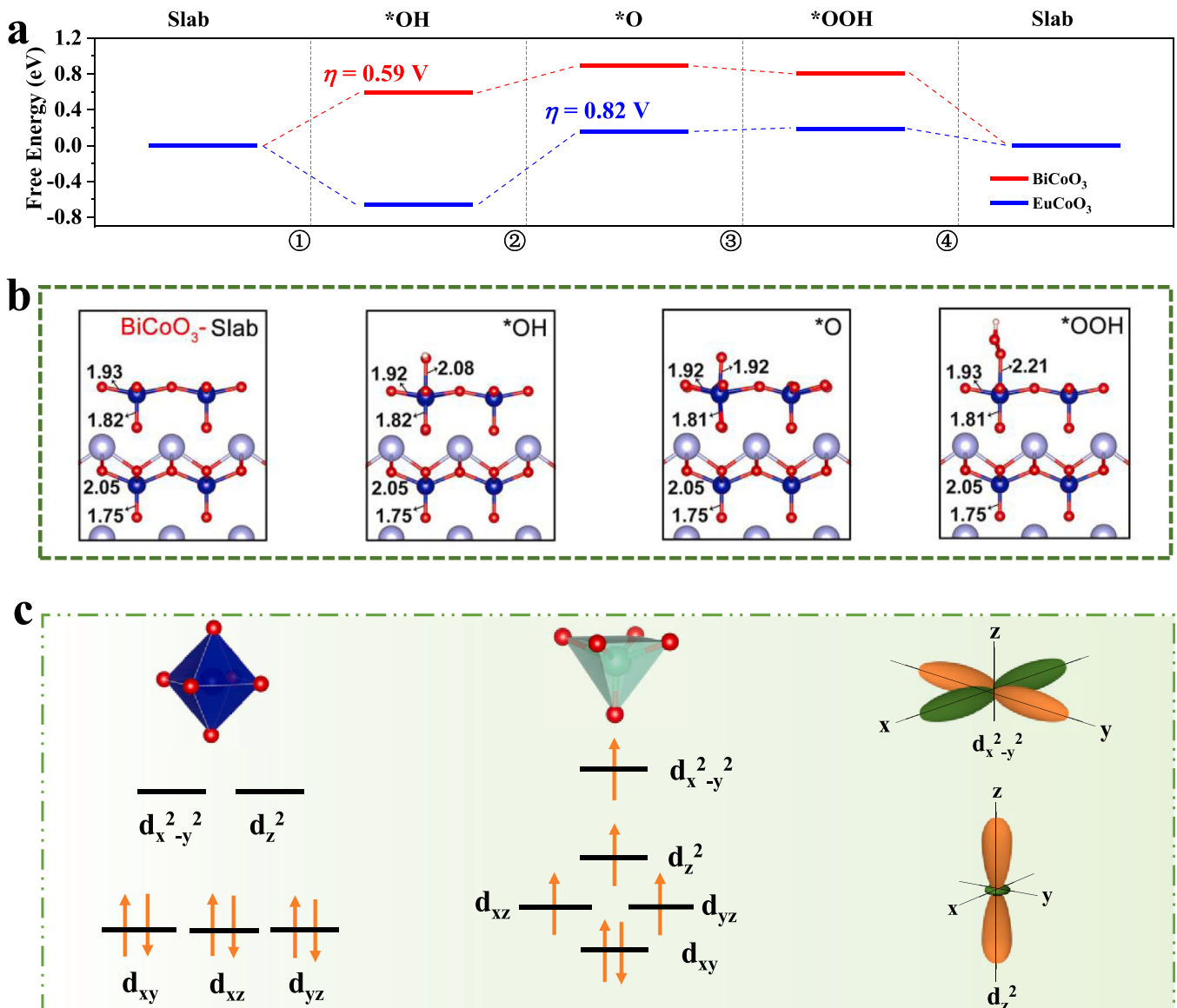


**Fig. 4.** a) Free energy diagrams for the OER via the MAE scenario for the BiCoO<sub>3</sub> and EuCoO<sub>3</sub> catalysts. b) Optimized structures of the OER adsorption intermediate corresponding to the MAE steps outlined in part (a) for the BiCoO<sub>3</sub>. Bond lengths of the various species (given in Å). c) The electronic configurations of the octahedrally-coordinated and pyramidal-coordinated Co ions and the  $d_{x^2-y^2}$  and  $d_z^2$  orbital shapes.

It is known that 3d electrons play a vital role in the OER process and we performed an analysis based on the decomposed density of states (DOS) [43] for each of the Co-3d levels in the pure BiCoO<sub>3</sub> and EuCoO<sub>3</sub> samples, which is plotted in Fig. S20. In the case of the Co<sup>3+</sup> component in the pristine EuCoO<sub>3</sub> (i.e., before the OER), the Co (3d<sup>6</sup>) configuration occupies the spin up and down channels of the t<sub>2g</sub> levels, i.e., the d<sub>xy</sub>, d<sub>xz</sub>, and d<sub>yz</sub> orbitals, which take part in strong bonding with the O 2p orbitals (Fig. S20a). The details of crystal-field splitting of 3d orbitals

with different coordinated structure are shown in Fig. 4c. For the Co<sup>3+</sup> component in the bulk BiCoO<sub>3</sub> (Fig. S20b), the Co t<sub>2g</sub> group further splits into d<sub>xy</sub> and a twofold degenerate level (d<sub>xz</sub> and d<sub>yz</sub>), while the Co e<sub>g</sub> group splits into d<sub>z</sub><sup>2</sup> and d<sub>xz</sub><sup>2</sup>, owing to the change in symmetry of the ligand field. In addition, in this Co<sup>3+</sup> (3d<sup>6</sup>) configuration of BiCoO<sub>3</sub>, the two spin-up and spin-down electrons occupy the d<sub>xy</sub> orbital, and the four majority spin electrons occupy the d<sub>xz</sub>, d<sub>yz</sub>, d<sub>z</sub><sup>2</sup>, and d<sub>xz</sub><sup>2</sup> levels, with unoccupied spin-down channels of d<sub>xz</sub>, d<sub>yz</sub>, d<sub>z</sub><sup>2</sup>, and d<sub>xz</sub><sup>2</sup>. This splitting of

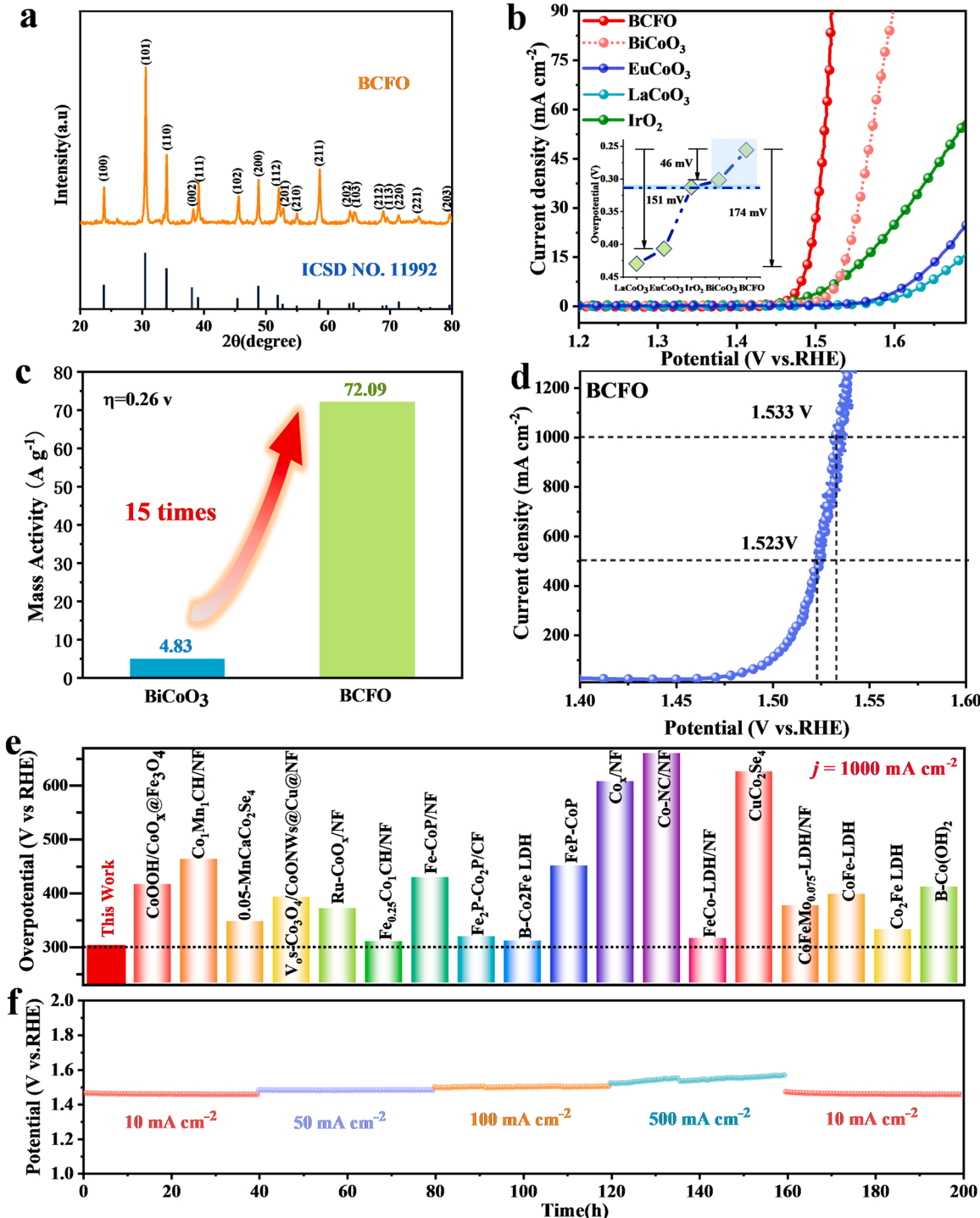


**Fig. 5.** a) XRD pattern of BCFO. b) OER LSV curves of BCFO, BiCoO<sub>3</sub>, EuCoO<sub>3</sub>, LaCoO<sub>3</sub> and IrO<sub>2</sub>. The illustration displays the overpotentials of the four samples at  $j = 10 \text{ mA cm}^{-2}$ . c) Mass activities at an overpotential of 0.26 V. d) LSV curves of BCFO during a high-current OER after coating on nickel foam. e) Comparison of the OER performances of BCFO and other reported Co-based oxide electrocatalysts at a large current density of  $1000 \text{ mA cm}^{-2}$ . f) Electrochemical stability of BCFO at different current densities of  $10, 50, 100, 500$ , and  $10 \text{ mA cm}^{-2}$  over a total of 200 h.

the 3d orbital in  $\text{BiCoO}_3$  was mainly attributed to Co and O hybridization. More specifically, as the Co–O bonds in the  $\text{CoO}_5$  coordination were elongated and deviated from the basal plane, the energy of  $d_{xy}^2$  orbital was pulled down by the reduced hybridization with the O 2p ligands. As shown in the right-hand side of Fig. 4c, the  $d_z^2$  orbital which is the  $\sigma$ -bonding  $e_g$  orbital, enables strong covalency between Co and oxygen-containing adsorbates, which directly promotes electron transfer between the surface Co species and the adsorbed intermediates, and play a significant role in the OER. Meanwhile, in the HS states, electrons occupation on more delocalized  $e_g$  orbital can promotes charge transport in the bulk [44–47], which is also beneficial to OER, especially for the case of the large current densities.

## 2.5. Generality and catalytic effectiveness of the structure of $\text{BiCoO}_3$

To evaluate the effectiveness and potential of this unique  $\text{CoO}_5$  pyramidal coordination structure of  $\text{BiCoO}_3$  for industrial water splitting, an alternative catalyst was prepared by partially replacing Co with the Fe (denoted BCFO), and studied its OER performance. The phase structure of the BCFO catalyst was examined by XRD (Fig. 5a), and it was confirmed that no impurity phase was observed, which is in echo with the results of TEM and Raman (Fig. S21). As shown in Fig. S22, the EDX elemental mapping depicted not only the dispersion of Bi, Co and O elements, but also the uniformly distribution of Fe elements, firmly demonstrating that Fe ions have been homogeneously incorporated in  $\text{BiCoO}_3$ . The XAFS measurement was performed to analyze the impact on Co after replaced by Fe. The Co K-edge XANES profile of BCFO is virtually identical to  $\text{BiCoO}_3$ , revealing the same coordinate environment of them, which is consistent with the above analysis (Fig. S23). In addition, the electrocatalytic OER activity of the Fe-incorporated sample was assessed via the polarization curves presented in Fig. 5b, wherein the inset displays the corresponding overpotential at a current density ( $j$ ) of  $10 \text{ mA cm}^{-2}$ . As can be seen from these results, the BCFO catalyst exhibited the lowest overpotential of 256 mV, which indicates the lowest degree of energy consumption for water splitting. In addition, BCFO was found to exhibit a high mass activity of  $72.09 \text{ A g}^{-1}$  at an overpotential of 0.26 V, which is  $\sim 15$  times higher than that of  $\text{BiCoO}_3$ , as outlined in Fig. 5c. Subsequently, to further evaluate the effectiveness of employing the BCFO catalyst in practical industrial applications, its OER performance was evaluated by coating on nickel foam. As shown in the LSV curves of BCFO towards OER (Fig. 5d), overpotentials of only 293 and 303 mV were required to afford the large current densities of 500 and  $1000 \text{ mA cm}^{-2}$ , respectively. The OER activity at large current densities of BCFO sample outperforms to those of any state-of-the-art Co-based catalyst reported to date, as summarized in Fig. 5e and Table S4. Simultaneously, the performance of BCFO catalyst was compared with that of other the state-of-the-art catalysts such as Ni–Fe LHDs and NiFeP-based materials, as shown in the Table S5, supporting that the performance of BCFO catalysts in this work belongs to the first-class level. The long-term electrochemical stability of BCFO was also evaluated under high-current-density operating conditions, wherein the electrode was tested at five constant current densities of 10, 50, 100, 500, and  $10 \text{ mA cm}^{-2}$  for a total of 200 h (Fig. 5f). During this operation, the extremely slow rate of activity decay demonstrated the excellent durability of this catalyst, and indicating its potential for industrial scale high-current-density water splitting applications. Furthermore, the experiments of EDX, Raman and TEM were carried out to investigate the structure of Co after the stability test. As shown in Fig. S24 and Fig. S25, it can be seen that the phase structure of BCFO almost remain unchanged, and the content of Co were remained after the stability test. Simultaneously, the chemical state of BCFO after the stability test was analysed by x-ray photoelectron spectroscopy (XPS) in Fig. S26. It was shown that the chemical state of Co ions remained the valence of + 3 [48,49], confirming the stability of catalyst BCFO.

## 2.6. Discussion of possible origin of large current densities in $\text{BiCoO}_3$

It is well known that the ideal electrochemical performance could be realized when the bonding strength between active site and adsorbate intermediate is moderate, and the too strong or too weak bonding strength would be not appropriate according to the Sabatier principle. First, introduction of oxygen vacancies can change the distribution of surface charge and optimizing the bonding strength of the oxygen intermediate to ideal level, which in turn elevate the OER activity of electrocatalysts as demonstrated by previous experiment and theoretical calculations [50–52]. Second, the common 3d transition metal oxide OER catalysts usually exhibit semiconductor behavior and thus the charge transfer and current-carrying capability is too insufficient to satisfy the demand of OER under large current densities. The intrinsic electrical conductivity can be improved by the formation of oxygen vacancies, which can reduce the band gap and enhance the density states across the Femi level leading to the fast electron transportation [53–55]. Third, OER would undergo a four-step process in alkaline media and there usually exist the limiting reaction barrier in one step, which can be determined as the rate-determining step. After generating oxygen vacancies, the energy barrier for the formation of intermediates in every step can be reduced and the rate-determining step would be further changed, which directly promote the OER process [55–57]. Fourth, the number of active sites for OER process can be dramatically increased accompanied by increasing the concentration of oxygen vacancies. As the active sites increasing, the distance between the nearest neighbors of sites becomes sufficiently short to provide the short OER reaction pathway, promoting the OER process [58,59]. With no need for the additional harsh-treatment like high temperature and vacuum condition,  $\text{BiCoO}_3$  inherently possess oxygen vacancies at every pyramidal high-spin  $\text{Co}^{3+}$  site, therefore this catalyst has the adequate active sites and the shortest reaction pathway leading to a high current density.

## 3. Conclusions

Herein, we successfully prepared a  $\text{BiCoO}_3$  catalyst with a pyramidal-coordinated  $\text{CoO}_5$  structure by means of a solid-state reaction, and subsequently, we investigated its crystal and electronic structures before and after its application in the oxygen evolution reaction (OER). Importantly, our  $\text{BiCoO}_3$  catalyst exhibited the low overpotentials of 391 and 402 mV to achieve the large current densities of 500 and  $1000 \text{ mA cm}^{-2}$ , respectively. Furthermore, even if the cobalt is replaced with Fe, this unique five-coordination configuration causes high OER performance with the 15-fold enhanced mass activity and only requires an ultralow overpotential of 303 mV to deliver a current density of  $1000 \text{ mA cm}^{-2}$ . Undergoing the deep exploration, it was found that the concentration of oxygen vacancies in  $\text{BiCoO}_3$  can reach up to 100% with ordered arrangement, which result in the shortest reaction pathway for oxygen intermediate and offer sufficient active sites for OER to intrinsically boost the performance. Overall, our work not only provides a highly active and stable OER electrocatalyst at industrial large current densities but also will be helpful in revealing the OER mechanism over the  $\text{CoO}_5$  catalyst.

## 4. Experimental

### 4.1. Catalyst preparation

**Preparation of the  $\text{BiCoO}_3$  and BCFO catalysts:**  $\text{BiCoO}_3$  was prepared using a solid-state reaction method.[18] More specifically,  $\text{Bi}_2\text{O}_3$ ,  $\text{Co}_3\text{O}_4$ , and  $\text{KClO}_4$  (1:2/3:3/4 molar ratio) were mixed homogeneously. The mixture was then pressed into pellets and subjected to high-pressure and high-temperature experiments at 5.5 GPa and 1373 K, respectively, over 30 min. After cooling to 25 °C, the sample was ground to a powder and then washed with deionized water several times to remove the residual KCl and yield the desired  $\text{BiCoO}_3$  powder. The BCFO catalyst was

prepared according to the above procedure with the exception that  $\text{Fe}_2\text{O}_3$  was added to the starting materials.

**Preparation of  $\text{EuCoO}_3$  and  $\text{LaCoO}_3$ :**  $\text{EuCoO}_3$  was prepared using a conventional sol-gel method. Initially, stoichiometric amounts of  $\text{Eu}(\text{NO}_3)_3 \cdot 6 \text{H}_2\text{O}$  and  $\text{Co}(\text{NO}_3)_2 \cdot 6 \text{H}_2\text{O}$  were dissolved in deionized water under stirring to form a homogeneous solution. Subsequently, EDTA and citric acid were added to the solution (1:2:1 molar ratio of EDTA / citric acid / total metal ions), and the pH was adjusted to 6 using an aqueous  $\text{NH}_3$  solution. The gel was obtained after evaporation and heated at 250 °C for 3 h to form a solid. Finally, the solid was calcined at 1000 °C for 8 h to produce the desired  $\text{EuCoO}_3$ . The  $\text{LaCoO}_3$  catalyst was prepared according to the above procedure with the exception that  $\text{La}(\text{NO}_3)_3 \cdot 6 \text{H}_2\text{O}$  was added to the starting materials.

#### 4.2. Material characterization

The powder XRD data were collected on a Bruker D8 Advance X-ray diffractometer with nickel-filtered Cu K $\alpha$  irradiation under a voltage and current of 40 kV and 40 mA, respectively. HRTEM and EDS were performed using an FEI Tecnai-G2 F20 instrument with an acceleration voltage of 200 kV. The XAFS spectra were acquired at the BL14W1 beamline of the Shanghai Synchrotron Radiation Facility (SSRF), Taiwan Light Source (TLS) beamline 17C1 and Taiwan Photon Source (TPS) beamline 44 A of the National Synchrotron Radiation Research Center (NSRRC). The energy for Co/Fe K-edges was calibrated according to the absorption edges of the corresponding foils, respectively. Furthermore, the soft XAS spectra (Co/Fe L<sub>2,3</sub>-edges and O K-edge) were recorded at the TLS-11A beamline of the NSRRC. The Raman spectra were recorded on a Horiba LabRAM HR Evolution instrument at an excitation wavelength of 473 nm, while the in situ Raman spectra were performed in a 0.1 M  $\text{K}^{16}\text{OH}$  ( $\text{H}_2^{18}\text{O}$ ) solution under altered potentials. The DEMS measurements were performed on a QAS-100 instrument equipped with a PrismaPro quadrupole mass spectrometer (Linglu Instruments) according to the following protocol: i) The catalyst was subjected to five CV cycles in a non-labeled 0.1 M KOH solution at a scan rate of 5 mV s<sup>-1</sup> to obtain the background signal; ii) the catalyst was labeled using a 0.1 M  $\text{K}^{16}\text{OH}$  ( $\text{H}_2^{18}\text{O}$ ) solution under the same conditions; iii) the catalyst was rinsed with  $\text{H}_2^{16}\text{O}$  to remove any residual  $\text{H}_2^{18}\text{O}$ , and the electrode was subjected to CV cycling in a 0.1 M  $\text{K}^{16}\text{OH}$  ( $\text{H}_2^{16}\text{O}$ ) solution. The gaseous products were collected and identified using mass spectroscopy.

#### 4.3. Electrochemical measurements

All electrochemical measurements were performed in  $\text{O}_2$ -saturated 1 M KOH using a three-electrode system on a Metrohm Autolab electrochemical workstation equipped with a PGSTAT 302 N system. A Hg/HgO electrode was served as the reference electrode, while a glassy carbon rotating disk electrode with a 5 mm diameter was used as the working electrode. The catalyst powder (5 mg) and the carbon black (5 mg) were dispersed in a mixed solution of deionized water and isopropanol (1 mL, 3:1, v/v). Nafion (40  $\mu\text{L}$ ) was then added to the mixture, and placed in an ultrasonic water bath for 2 h. The resulting catalyst ink (8  $\mu\text{L}$ ) was added dropwise onto the polished glassy carbon electrode to give a catalyst loading of 0.196 mg cm<sup>-2</sup>, and the working electrode was allowed to dry naturally before testing. The LSVs were obtained at a scan rate of 5 mV s<sup>-1</sup>, and the potentials were converted to reversible hydrogen electrode (RHE) values according to the equation  $E(\text{RHE}) = E(\text{Hg/HgO}) + 0.059 \text{ pH} + 0.096 \text{ V}$ . The compensation of resistance was based on manual iR-correction. Furthermore, the electrodes which were tested under high-current densities can be prepared by spreading the abovementioned ink on 0.5 cm<sup>-2</sup> NF.

#### 4.4. Density function theory calculations

For the purpose of this study, the Vienna ab initio simulation package

(VASP) [60,61] was used to carry out the DFT calculations in conjunction with projector augmented wave (PAW) formalism. The H 1 s<sup>1</sup>, O 2 s<sup>2</sup>2p<sup>4</sup>, Bi 6 s<sup>2</sup>6p<sup>3</sup>, Eu 5p<sup>6</sup>6 s<sup>2</sup>, and Co 4 s<sup>2</sup>3d<sup>7</sup> states were treated as the valence electrons. The electronic wave functions were expanded in plane waves using an energy cut-off of 500 eV, and the force and energy convergence criteria were set to 0.02 eV Å<sup>-1</sup> and 10<sup>-5</sup> eV respectively. As previously reported,  $\text{BiCoO}_3$  should be categorized as a Mott insulator due to its band gap of ~1.7 eV [62,63]. Thus, to accurately evaluate the electronic properties of  $\text{BiCoO}_3$ , the Hubbard U model [64] was employed to describe the strong correlation of the localized Co 3d states, and the values of U and the Hund exchange J were set to 6 and 0.9 eV, respectively, i.e., effective  $U_{\text{eff}} = U - J = 5.10$  eV, according to a previous study [65]. The reciprocal space was sampled using a 4 × 4 × 1 Monkhorst-Pack k-point mesh for DFT+U calculations. To prevent spurious interactions, the thickness of the vacuum spacing was set to ~15 Å in the z-direction. The Gibbs free energy differences ( $\Delta G$ ) were calculated using the computational hydrogen electrode model under standard conditions [66] with applied voltages of  $U_{\text{RHE}} = 0$  and 1.23 V. The calculation details for  $\Delta G$  are provided in the Supporting Information. To highlight the charge redistribution between surface and subsurface, the electronic charge differences are calculated based on  $\rho(\mathbf{r}) = \rho(\text{slab}) - \rho(\text{surface}) - \rho(\text{slab without surface})$ , and the plane-integrated electron density differences are calculated according to  $\Delta\rho(Z) = \iint \Delta\rho(x, y, z) dx dy$ .

#### CRediT authorship contribution statement

**Yitian Hu:** Investigation, Methodology, Visualization, Data curation, Validation, Writing – original draft. **Lili Li:** DFT calculation, Formal analysis, Funding acquisition. **Jianfa Zhao:** Data curation, Formal analysis. **Yu-Cheng Huang:** Data curation, Formal analysis. **Changyang Kuo:** Data curation, Formal analysis. **Jing Zhou:** Writing – review & editing, DFT calculation, Formal analysis, Funding acquisition. **Yalei Fan:** DFT calculation, Formal analysis. **Hong-Ji Lin:** Data curation, Visualization. **Chung-Li Dong:** Data curation, Formal analysis. **Chih-Wen Pao:** Data curation, Formal analysis. **Jyh-Fu Lee:** Data curation, Formal analysis. **Chien-Te Chen:** Data curation, Formal analysis. **Changqing Jin:** Data curation, Formal analysis. **Zhiwei Hu:** Conceptualization, Visualization, Writing-review & editing, Supervision. **Jian-Qiang Wang:** Project administration, Supervision, Funding acquisition. **Linjuan Zhang:** Writing – review & editing, Supervision, Funding acquisition, Writing – review & editing.

#### Declaration of Competing Interest

The authors declare that they have no known competing financial interests or personal relationships that could have appeared to influence the work reported in this paper.

#### Data availability

Data will be made available on request.

#### Acknowledgement

This work was financially supported by National Key R&D Program of China (2021YFA1502400, 2022YFB4002502), the “Transformational Technologies for Clean Energy and Demonstration,” Strategic Priority Research Program of the Chinese Academy of Sciences (Grant No. XDA2100000), the National Science Foundation of China (Grant No. 22179141, and No.22209201), Youth Innovation Promotion Association, Chinese Academy of Science (Grant No. 2022257), DNL Cooperation Fund, CAS (Grant No. DNL202008) and the Photon Science Center for Carbon Neutrality. We acknowledge the support from the Max Planck-POSTECH-Hsinchu Center for Complex Phase Materials.

## Appendix A. Supporting information

Supplementary data associated with this article can be found in the online version at doi:10.1016/j.apcatb.2023.122785.

## References

- [1] Z. Xue, Y. Li, Y. Zhang, W. Geng, B. Jia, J. Tang, S. Bao, H.-P. Wang, Y. Fan, Z.-W. Wei, Z. Zhang, Z. Ke, G. Li, C.-Y. Su, Modulating electronic structure of metal-organic framework for efficient electrocatalytic oxygen evolution, *Adv. Energy Mater.* 8 (2018) 1801564.
- [2] Y. Xu, B. Li, S. Zheng, P. Wu, J. Zhan, H. Xue, Q. Xu, H. Pang, Ultrathin two-dimensional cobalt-organic framework nanosheets for high-performance electrocatalytic oxygen evolution, *J. Mater. Chem. A* 6 (2018) 22070.
- [3] S. Song, J. Zhou, S. Zhang, L. Zhang, J. Li, Y. Wang, L. Han, Y. Long, Z. Hu, J.-Q. Wang, Molten-salt synthesis of porous La<sub>0.6</sub>Sr<sub>0.4</sub>Co<sub>0.2</sub>Fe<sub>0.8</sub>O<sub>2.9</sub> perovskite as an efficient electrocatalyst for oxygen evolution, *Nano Res.* 11 (2018) 4796–4805.
- [4] Y. Xu, C. Wang, Y. Huang, J. Fu, Recent advances in electrocatalysts for neutral and large-current-density water electrolysis, *Nano Energy* 80 (2021), 105545.
- [5] S. Hu, S. Ge, H. Liu, X. Kang, Q. Yu, B. Liu, Low-dimensional electrocatalysts for acidic oxygen evolution: intrinsic activity, high current density operation, and long-term stability, *Adv. Funct. Mater.* 32 (2022) 2201726.
- [6] X. Zhang, M. Jin, F. Jia, J. Huang, A. Amini, S. Song, H. Yi, C. Cheng, Noble-metal-free OER electrocatalysts working at high current densities over 1000 mA cm<sup>-2</sup>: From fundamental understanding to design principles, *Energy Environ. Mater.* 0 (2022), e12457.
- [7] P. Liu, B. Chen, C. Liang, W. Yao, Y. Cui, S. Hu, P. Zou, H. Zhang, H.J. Fan, C. Yang, Tip-enhanced electric field: a new mechanism promoting mass transfer in oxygen evolution reactions, *Adv. Mater.* 33 (2021) 2007377.
- [8] Q. Wen, K. Yang, D. Huang, G. Cheng, X. Ai, Y. Liu, J. Fang, H. Li, L. Yu, T. Zhai, Schottky heterojunction nanosheet array achieving high-current-density oxygen evolution for industrial water splitting electrolyzers, *Adv. Energy Mater.* 11 (2021) 2102353.
- [9] C. Liang, P. Zou, A. Nairan, Y. Zhang, J. Liu, K. Liu, S. Hu, F. Kang, H.J. Fan, C. Yang, Exceptional performance of hierarchical Ni–Fe oxyhydroxide@NiFe alloy nanowire array electrocatalysts for large current density water splitting, *Energy Environ. Sci.* 13 (2020) 86–95.
- [10] X. Yu, M. Wang, X. Gong, Z. Guo, Z. Wang, S. Jiao, Self-supporting porous Co-based films with phase-separation structure for ultrastable overall water electrolysis at large current density, *Adv. Energy Mater.* 8 (2018) 1802445.
- [11] Y. Hu, J. Zhou, L. Li, Z. Hu, t yuan, C. Jing, R. Liu, S. Xi, H. Jiang, J.-Q. Wang, L. Zhang, Dynamic structural transformation induced by defects in nano-rod FeOOH during electrochemical water splitting, *J. Mater. Chem. A* 10 (2022) 602.
- [12] Z. Xiao, Y. Wang, Y.-C. Huang, Z. Wei, C.-L. Dong, J. Ma, S. Shen, Y. Li, S. Wang, Filling the oxygen vacancies in Co<sub>3</sub>O<sub>4</sub> with phosphorus: an ultra-efficient electrocatalyst for overall water splitting, *Energy Environ. Sci.* 10 (2017) 2563–2569.
- [13] Z. Xiao, Y.C. Huang, C.L. Dong, C. Xie, Z. Liu, S. Du, W. Chen, D. Yan, L. Tao, Z. Shu, G. Zhang, H. Duan, Y. Wang, Y. Zou, R. Chen, S. Wang, Operando identification of the dynamic behavior of oxygen vacancy-rich Co<sub>3</sub>O<sub>4</sub> for oxygen evolution reaction, *J. Am. Chem. Soc.* 142 (2020) 12087–12095.
- [14] T. Liu, A. Li, W. Zhou, C. Lyu, Hierarchical nano/micro/macro-assembled integrated electrode with high-performance water electro-oxidation, *Chem. Eng. J.* 415 (2021), 128941.
- [15] X. Xu, Y. Pan, L. Ge, Y. Chen, X. Mao, D. Guan, M. Li, Y. Zhong, Z. Hu, V. K. Peterson, M. Saunders, C.T. Chen, H. Zhang, R. Ran, A. Du, H. Wang, S.P. Jiang, W. Zhou, Z. Shao, High-Performance Perovskite Composites Electrocatalysts Enabled by Controllable Interface Engineering, *Small* 17 (2021) 2101573.
- [16] Z.W. Seh, J. Kibsgaard, C.F. Dickens, I. Chorkendorff, J.K. Norskov, T.F. Jaramillo, Combining theory and experiment in electrocatalysis: Insights into materials design, *Science* 355 (2017) 146.
- [17] J. Suntivich, J. May Kevin, A. Gasteiger Hubert, B. Goodenough John, Y. Shao-Horn, A. Perovskite, Oxide Optimized for Oxygen Evolution Catalysis from Molecular Orbital Principles, *Science* 334 (2011) 1383–1385.
- [18] J. Zhao, S.-C. Haw, X. Wang, Z. Hu, C.-Y. Kuo, S.-A. Chen, H. Ishii, N. Hiraoka, H.-J. Lin, C.-T. Chen, Z. Li, A. Tanaka, C.-E. Liu, R. Yu, J.-M. Chen, C. Jin, Spin State and Spin-State Transition of Co<sup>3+</sup> Ion in BiCo<sub>3</sub>, *Phys. Status Solidi B* 258 (2021) 2100117.
- [19] X. Lin, Y.C. Huang, Z. Hu, L. Li, J. Zhou, Q. Zhao, H. Huang, J. Sun, C.W. Pao, Y. C. Chang, H.J. Lin, C.T. Chen, C.L. Dong, J.Q. Wang, L. Zhang, 5f Covalency Synergistically Boosting Oxygen Evolution of UCo<sub>4</sub> Catalyst, *J. Am. Chem. Soc.* 144 (2022) 416–423.
- [20] L. Li, H. Sun, Z. Hu, J. Zhou, Y.C. Huang, H. Huang, S. Song, C.W. Pao, Y.C. Chang, A.C. Komarek, H.J. Lin, C.T. Chen, C.L. Dong, J.Q. Wang, L. Zhang, In Situ/Operando Capturing Unusual Ir<sup>6+</sup> Facilitating Ultrafast Electrocatalytic Water Oxidation, *Adv. Funct. Mater.* 31 (2021) 2104746.
- [21] W. Huang, J. Li, X. Liao, R. Lu, C. Ling, X. Liu, J. Meng, L. Qu, M. Lin, X. Hong, X. Zhou, S. Liu, Y. Zhao, L. Zhou, L. Mai, Ligand Modulation of Active Sites to Promote Electrocatalytic Oxygen Evolution, *Adv. Mater.* 34 (2022) 2200270.
- [22] L.J. Zhang, J.Q. Wang, J. Li, J. Zhou, W.P. Cai, J. Cheng, W. Xu, G. Yin, X. Wu, Z. Jiang, S. Zhang, Z.Y. Wu, High-Tc ferromagnetism in a Co-doped ZnO system dominated by the formation of a zinc-blende type Co-rich ZnCo<sub>2</sub> phase, *Chem. Commun.* 48 (2012) 91–93.
- [23] C. Si, W. Xu, H. Wang, J. Zhou, A. Ablat, L. Zhang, J. Cheng, Z. Pan, L. Fan, C. Zou, Z. Wu, Metal-insulator transition in V<sub>1-x</sub>W<sub>x</sub>O<sub>3</sub>: structural and electronic origin, *Phys. Chem. Chem. Phys.* 14 (2012) 15021–15028.
- [24] Z. Hu, H. Wu, M.W. Haverkort, H.H. Hsieh, H.J. Lin, T. Lorenz, J. Baier, A. Reichl, I. Bonn, C. Felser, A. Tanaka, C.T. Chen, L.H. Tjeng, Different look at the spin state of Co<sup>3+</sup> ions in a Co<sub>3</sub>O<sub>4</sub> pyramidal coordination, *Phys. Rev. Lett.* 92 (2004), 207402.
- [25] P.G. Radaelli, S.W. Cheong, Structural phenomena associated with the spin-state transition in LaCoO<sub>3</sub>, *Phys. Rev. B* 66 (2002), 094408.
- [26] J. Zhou, J. Li, L. Zhang, S. Song, Y. Wang, X. Lin, S. Gu, X. Wu, T.-C. Weng, J. Wang, S. Zhang, Highly Active Surface Structure in Nanosized Spinel Cobalt-Based Oxides for Electrocatalytic Water Splitting, *J. Phys. Chem. C* 122 (2018) 14447–14458.
- [27] M.W. Haverkort, Z. Hu, J.C. Cezar, T. Burnus, H. Hartmann, M. Reuther, C. Zobel, T. Lorenz, A. Tanaka, N.B. Brookes, H.H. Hsieh, H.J. Lin, C.T. Chen, L.H. Tjeng, Spin state transition in LaCoO<sub>3</sub> studied using soft x-ray absorption spectroscopy and magnetic circular dichroism, *Phys. Rev. Lett.* 97 (2006), 176405.
- [28] D. Takegami, A. Tanaka, S. Agrestini, Z. Hu, J. Weinen, M. Rotter, C. Schüller-Langeheine, T. Willers, T.C. Koethe, T. Lorenz, Y.F. Liao, K.D. Tsuei, H.J. Lin, C. T. Chen, L.H. Tjeng, Paramagnetic LaCoO<sub>3</sub>: a highly inhomogeneous mixed spin-state system, *Phys. Rev. X* 13 (2023), 011037.
- [29] Y.Y. Chin, Z. Hu, Y. Su, Y. Tsujimoto, A. Tanaka, C.T. Chen, Experimental and theoretical soft X-ray absorption study on Co<sup>3+</sup> ion spin states in Sr<sub>2-x</sub>Ca<sub>x</sub>Co<sub>3</sub>F, *Phys. Status Solidi RRL* 12 (2018) 1800147.
- [30] Y.Y. Chin, H.J. Lin, Z. Hu, C.Y. Kuo, D. Mikhailova, J.M. Lee, S.C. Haw, S.A. Chen, W. Schnelle, H. Ishii, N. Hiraoka, Y.F. Liao, K.D. Tsuei, A. Tanaka, L. Hao Tjeng, C. T. Chen, J.M. Chen, Relation between the Co-O bond lengths and the spin state of Co in layered Cobaltates: a high-pressure study, *Sci. Rep.* 7 (2017) 3656.
- [31] K. Feng, D. Zhang, F. Liu, H. Li, J. Xu, Y. Xia, Y. Li, H. Lin, S. Wang, M. Shao, Z. Kang, J. Zhong, Highly Efficient Oxygen Evolution by a Thermocatalytic Process Cascaded Electrocatalysis Over Sulfur-Treated Fe-Based Metal-Organic-Frameworks, *Adv. Energy Mater.* 10 (2020) 2000184.
- [32] H. Huang, W. Huang, Z. Yang, J. Huang, J. Lin, W. Liu, Y. Liu, Strongly coupled MoS<sub>2</sub> nanoflake–carbon nanotube nanocomposite as an excellent electrocatalyst for hydrogen evolution reaction, *J. Mater. Chem. A* 5 (2017) 1558.
- [33] A. Grimaud, O. Diaz-Morales, B. Han, W.T. Hong, Y.L. Lee, L. Giordano, K. A. Stoerzinger, M.T.M. Koper, Y. Shao-Horn, Activating lattice oxygen redox reactions in metal oxides to catalyse oxygen evolution, *Nat. Chem.* 9 (2017) 457–465.
- [34] S. Zhou, X. Miao, X. Zhao, C. Ma, Y. Qiu, Z. Hu, J. Zhao, L. Shi, J. Zeng, Engineering electrocatalytic activity in nanosized perovskite cobaltite through surface spin-state transition, *Nat. Commun.* 7 (2016) 11510.
- [35] Z. Hu, H. Wu, T.C. Koethe, S.N. Barilo, S.V. Shiryaev, G.L. Bychkov, C. Schüller-Langeheine, T. Lorenz, A. Tanaka, H.H. Hsieh, H.J. Lin, C.T. Chen, N.B. Brookes, S. Agrestini, Y.Y. Chin, M. Rotter, L.H. Tjeng, Spin-state order/disorder and metal-insulator transition in GdBa<sub>2</sub>Co<sub>3</sub>O<sub>5.5</sub>: experimental determination of the underlying electronic structure, *N. J. Phys.* 14 (2012), 123025.
- [36] C.F. Chang, Z. Hu, H. Wu, T. Burnus, N. Hollmann, M. Benomar, T. Lorenz, A. Tanaka, H.J. Lin, H.H. Hsieh, C.T. Chen, L.H. Tjeng, Spin blockade, orbital occupation, and charge ordering in La<sub>1.5</sub>Sr<sub>0.5</sub>CoO<sub>4</sub>, *Phys. Rev. Lett.* 102 (2009), 116401.
- [37] N. Hollmann, Z. Hu, M. Valldor, A. Maignan, A. Tanaka, H.H. Hsieh, H.J. Lin, C. T. Chen, L.H. Tjeng, Electronic and magnetic properties of the kagome systems YBa<sub>2</sub>Co<sub>3</sub>O<sub>7</sub> and YBa<sub>2</sub>Co<sub>3</sub>Mo<sub>7</sub>(M=Al, Fe), *Phys. Rev. B* 80 (2009), 085111.
- [38] T. Burnus, Z. Hu, M.W. Haverkort, J.C. Cezar, D. Flahaut, V. Hardy, A. Maignan, N. B. Brookes, A. Tanaka, H.H. Hsieh, H.J. Lin, C.T. Chen, L.H. Tjeng, Valence, spin, and orbital state of Co ions in one-dimensional Ca<sub>3</sub>Co<sub>2</sub>O<sub>6</sub>: an x-ray absorption and magnetic circular dichroism study, *Phys. Rev. B* 74 (2006), 245111.
- [39] Y.Y. Chin, Z. Hu, H.J. Lin, S. Agrestini, J. Weinen, C. Martin, S. Hébert, A. Maignan, A. Tanaka, J.C. Cezar, N.B. Brookes, Y.F. Liao, K.D. Tsuei, C.T. Chen, D.I. Khomskii, L.H. Tjeng, Spin-orbit coupling and crystal-field distortions for a low-spin 3d<sup>5</sup> state in BaCoO<sub>3</sub>, *Phys. Rev. B* 100 (2019), 205139.
- [40] T. Sudayama, Y. Wakisaka, H. Wadati, G.A. Sawatzky, D. G. Hawthorn, T.Z. Regier, K. Oka, M. Azuma, Y. Shimakawa, Co–O–O–Co superexchange pathways enhanced by small charge-transfer energy in multiferroic BiCoO<sub>3</sub>, *Phys. Rev. B* 83 (2011), 235105.
- [41] J. Zhou, Y. Hu, Y.-C. Chang, Z. Hu, Y.-C. Huang, Y. Fan, H.-J. Lin, C.-W. Pao, C.-L. Dong, J.-F. Lee, C.-T. Chen, J.-Q. Wang, L. Zhang, In situ exploring of the origin of the enhanced oxygen evolution reaction efficiency of metal(Co/Fe)-organic framework catalysts via postprocessing, *ACS Catal.* 12 (2022) 3138–3148.
- [42] K. Oka, M. Azuma, W.-t Chen, H. Yusa, A.A. Belik, E. Takayama-Muromachii, M. Mizumaki, N. Ishimatsu, N. Hiraoka, M. Tsujimoto, M.G. Tucker, J.P. Attfield, Y. Shimakawa, Pressure-Induced Spin-State Transition in BiCoO<sub>3</sub>, *J. Am. Chem. Soc.* 132 (2010) 9438–9443.
- [43] J. Zhou, H. Li, L. Zhang, J. Cheng, H. Zhao, W. Chu, J. Yang, Y. Luo, Z. Wu, Tuning magnetism in transition-metal-doped 3C silicon carbide polytype, *J. Phys. Chem. C* 115 (2011) 253–256.
- [44] Y. Duan, S. Sun, S. Xi, X. Ren, Y. Zhou, G. Zhang, H. Yang, Y. Du, Z.J. Xu, Tailoring the Co 3d–O 2p Covalency in LaCoO<sub>3</sub> by Fe Substitution To Promote Oxygen Evolution Reaction, *Chem. Mater.* 29 (2017) 10534–10541.
- [45] H. Zhong, X. Wang, G. Sun, Y. Tang, S. Tan, Q. He, J. Zhang, T. Xiong, C. Diao, Z. Yu, S. Xi, W.S.V. Lee, J. Xue, Optimization of oxygen evolution activity by tuning e<sup>g</sup> band broadening in nickel oxyhydroxide, *Energy Environ. Sci.* 16 (2023) 641–652.
- [46] Y. Tong, Y. Guo, P. Chen, H. Liu, M. Zhang, L. Zhang, W. Yan, W. Chu, C. Wu, Y. Xie, Spin-state regulation of perovskite cobaltite to realize enhanced oxygen evolution activity, *Chem* 3 (2017) 812–821.

- [47] J. Qian, T. Wang, Z. Zhang, Y. Liu, J. Li, D. Gao, Engineered spin state in Ce doped LaCo<sub>3</sub> with enhanced electrocatalytic activity for rechargeable Zn-Air batteries, *Nano Energy* 74 (2020), 104948.
- [48] Y. Sun, X. Ren, S. Sun, Z. Liu, S. Xi, Z.J. Xu, Engineering high-spin state cobalt cations in spinel zinc cobalt oxide for spin channel propagation and active site enhancement in water oxidation, *Angew. Chem. Int. Ed.* 60 (2021) 14536–14544.
- [49] Y.A. Teterin, A.V. Sobolev, A.A. Belik, Y.S. Glazkova, K.I. Maslakov, V. G. Yarzhemskii, A.Y. Teterin, K.E. Ivanov, I.A. Presnyakov, Electronic structure of cobaltites ScCo<sub>1-x</sub>Fe<sub>x</sub>O<sub>3</sub> ( $x = 0, 0.05$ ) and BiCoO<sub>3</sub>: X-ray photoelectron spectroscopy, *J. Exp. Theor. Phys.* 128 (2019) 899–908.
- [50] X. Zhang, Y. Zhao, Y. Zhao, R. Shi, G.I.N. Waterhouse, T. Zhang, A simple synthetic strategy toward defect-rich porous monolayer NiFe-layered double hydroxide nanosheets for efficient electrocatalytic water oxidation, *Adv. Energy Mater.* 9 (2019) 1900881.
- [51] C. Hu, X. Wang, T. Yao, T. Gao, J. Han, X. Zhang, Y. Zhang, P. Xu, B. Song, Enhanced electrocatalytic oxygen evolution activity by tuning both the oxygen vacancy and orbital occupancy of B-site metal cation in NdNiO<sub>3</sub>, *Adv. Funct. Mater.* 29 (2019) 1902449.
- [52] Y. Liu, G. Chen, R. Ge, K. Pei, C. Song, W. Li, Y. Chen, Y. Zhang, L. Feng, R. Che, Construction of CoNiFe Trimetallic Carbonate Hydroxide Hierarchical Hollow Microflowers with Oxygen Vacancies for Electrocatalytic Water Oxidation, *Adv. Funct. Mater.* 32 (2022) 2200726.
- [53] F. Nur Indah Sari, S. Abdillah, J.-M. Ting, FeOOH-containing hydrated iron vanadate electrocatalyst for superior oxygen evolution reaction and efficient water splitting, *Chem. Eng. J.* 416 (2021), 129165.
- [54] H. Xu, Z.-X. Shi, Y.-X. Tong, G.-R. Li, Porous microrod arrays constructed by carbon-confined NiCo@NiCo<sub>2</sub>O<sub>4</sub> Core@Shell nanoparticles as efficient electrocatalysts for oxygen evolution, *Adv. Mater.* 30 (2018) 1705442.
- [55] B. Zhang, J. Shan, X. Wang, Y. Hu, Y. Li, Ru/Rh Cation Doping and Oxygen-Vacancy Engineering of FeOOH Nanoarrays@Ti<sub>3</sub>C<sub>2</sub>T<sub>x</sub> MXene Heterojunction for Highly Efficient and Stable Electrocatalytic Oxygen Evolution, *Small* 18 (2022) 2200173.
- [56] S. Peng, F. Gong, L. Li, D. Yu, D. Ji, T. Zhang, Z. Hu, Z. Zhang, S. Chou, Y. Du, S. Ramakrishna, Necklace-like multishelled hollow spinel oxides with oxygen vacancies for efficient water electrolysis, *J. Am. Chem. Soc.* 140 (2018) 13644–13653.
- [57] K. Zhang, G. Zhang, J. Qu, H. Liu, Disordering the Atomic Structure of Co(II) Oxide via B-Doping: An Efficient Oxygen Vacancy Introduction Approach for High Oxygen Evolution Reaction Electrocatalysts, *Small* 14 (2018) 1802760.
- [58] S. Hirai, K. Morita, K. Yasuoka, T. Shibuya, Y. Tojo, Y. Kamihara, A. Miura, H. Suzuki, T. Ohno, T. Matsuda, S. Yagi, Oxygen vacancy-originated highly active electrocatalysts for the oxygen evolution reaction, *J. Mater. Chem. A* 6 (2018) 15102–15109.
- [59] D. Guan, J. Zhou, Z. Hu, W. Zhou, X. Xu, Y. Zhong, B. Liu, Y. Chen, M. Xu, H.J. Lin, C.T. Chen, J.Q. Wang, Z. Shao, Searching general sufficient-and-necessary conditions for ultrafast hydrogen-evolving electrocatalysis, *Adv. Funct. Mater.* 29 (2019) 1900704.
- [60] J.P. Perdew, K. Burke, M. Ernzerhof, Generalized gradient approximation made simple, *Phys. Rev. Lett.* 77 (1996) 3865–3868.
- [61] G. Kresse, J. Furthmüller, Efficient iterative schemes for ab initio total-energy calculations using a plane-wave basis set, *Phys. Rev. B* 54 (1996) 11169–11186.
- [62] J.A. McLeod, Z.V. Pchelkina, L.D. Finkelstein, E.Z. Kurmaev, R.G. Wilks, A. Moewes, I.V. Solovyev, A.A. Belik, E. Takayama-Muromachi, Electronic structure of BiMo<sub>3</sub> multiferroics and related oxides, *Phys. Rev. B* 81 (2010), 144103.
- [63] A.A. Belik, S. Iikubo, K. Kodama, N. Igawa, S.-i Shamoto, S. Niitaka, M. Azuma, Y. Shimakawa, M. Takano, F. Izumi, E. Takayama-Muromachi, Neutron powder diffraction study on the crystal and magnetic structures of BiCoO<sub>3</sub>, *Chem. Mater.* 18 (2006) 798–803.
- [64] S.L. Dudarev, G.A. Botton, S.Y. Savrasov, C.J. Humphreys, A.P. Sutton, Electron-energy-loss spectra and the structural stability of nickel oxide: an LSDA+U study, *Phys. Rev. B* 57 (1998) 1505–1509.
- [65] T. Jia, H. Wu, G. Zhang, X. Zhang, Y. Guo, Z. Zeng, H.-Q. Lin, Ab initio study of the giant ferroelectric distortion and pressure-induced spin-state transition in BiCoO<sub>3</sub>, *Phys. Rev. B* 83 (2011), 174433.
- [66] M. Bajdich, M. García-Mota, A. Vojvodic, J.K. Nørskov, A.T. Bell, Theoretical investigation of the activity of cobalt oxides for the electrochemical oxidation of water, *J. Am. Chem. Soc.* 135 (2013) 13521–13530.